

3 INFERENCE OF HEATING PROPERTIES FROM “HOT” NON-FLARING PLASMAS IN ACTIVE REGION
4 CORES II. NANOFLARE TRAINS

5 W. T. BARNES¹, P. J. CARGILL^{2,3}, AND S. J. BRADSHAW¹

¹Department of Physics & Astronomy, Rice University, Houston, TX 77251-1892; will.t.barnes@rice.edu, stephen.bradshaw@rice.edu

²Space and Atmospheric Physics, The Blackett Laboratory, Imperial College, London SW7 2BW; p.cargill@imperial.ac.uk

³School of Mathematics and Statistics, University of St Andrews, St Andrews, Scotland KY16 9SS

ABSTRACT

Faint, high-temperature emission in active region cores has long been predicted as a signature of nanoflare heating. However, the detection of such emission has proved difficult due to a combination of the efficiency of thermal conduction, non-equilibrium ionization, and inadequate instrument sensitivity. In this second paper in our series on “hot” non-flaring plasma in active regions, we investigate the influence of repeating nanoflares of varying frequency on the resulting emission measure distribution. We have used an efficient two-fluid hydrodynamic model to carry out a parameter exploration in preferentially heated species, heating event frequency, and the power-law index determining the distribution of event energies. We compute the emission measure distribution for each point in our multi-dimensional heating parameter space in an effort to understand how each of these variables impacts the observed emission. Additionally, we calculate several observables and compare their efficacy in capturing the character of both the hot and cool parts of the emission measure distribution.

Keywords: Sun:corona, Sun:nanoflares, plasmas, hydrodynamics

1. INTRODUCTION

Collaboration note: Maybe intro is a bit lengthy...where to cut it down?

The concept of heating the solar corona by nanoflares, first proposed by Parker (1988), has been developed extensively over the past two decades (e.g. Cargill 1994; Cargill & Klimchuk 2004; Klimchuk 2006). The term *nanoflare* has now become synonymous with impulsive heating in the energy range $10^{24} - 10^{27}$ erg, with no specific assumption regarding the underlying physical mechanism (for example, small-scale magnetic reconnection or hydromagnetic wave dissipation). In active region (AR) cores such as those we discuss in this paper, one strategy for constraining potential heating models is the analysis of the emission measure distribution as a function of temperature, $EM(T) = \int n^2 dh$. Cargill (1994); Cargill & Klimchuk (2004) predicted that $EM(T)$ resulting from nanoflare heating should be wide, with a maximum value at $T = T_m \sim 10^{6.5}$ K and have a faint, high-temperature (8-10 MK) component. Below T_m , there is a scaling $EM(T) \sim T^a$ over a temperature range $10^6 \lesssim T \lesssim T_m$, a result first discussed by Jordan (1975). Observations from the *Hinode* spacecraft (Kosugi et al. 2007) have shown that $2 \lesssim a \lesssim 5$, with $T_m \approx 10^{6.5-6.6}$ (Warren et al. 2011, 2012; Winebarger et al. 2011; Tripathi et al. 2011; Schmelz & Pathak 2012; Del Zanna et al. 2015).

The emission component above T_m has been the subject of less study, but is likely to be important as the so-called “smoking gun” of nanoflare heating since its properties may bear a close link to the actual heating. While many workers (Reale et al. 2009; Schmelz et al. 2009; Miceli et al. 2012; Testa & Reale 2012; Del Zanna & Mason 2014; Petralia et al. 2014; Schmelz et al. 2015) have claimed evidence of this hot, faint component of the emission measure, poor spectral resolution (Testa et al. 2011; Winebarger et al. 2012) and non-equilibrium ionization (Bradshaw & Cargill 2006; Reale & Orlando 2008) have made a positive detection of nanoflare heating difficult. However, Brosius et al. (2014) used observations from the *EUNIS-13* sounding rocket to identify relatively faint emission from Fe XIX in a non-flaring active region (AR), suggesting temperatures of ~ 8.9 MK.

A scaling has been claimed for hot emission with $T > T_m$ such that $EM \propto T^{-b}$, with $b > 0$. This fit is usually done in the range $T_m \lesssim T \lesssim 10^{7.2}$. However, measured values of these “hotward” slopes are poorly constrained due to both the low magnitude of emission and the lack of available spectroscopic data in this temperature range (Winebarger et al. 2012). Warren et al. (2012), find $7 \lesssim b \lesssim 10$, with uncertainties of $\pm 2.5 - 3$, for 15 AR cores though Del Zanna & Mason (2014), using observations from the Solar Maximum Mission,

claim larger values for b . It must be noted though that reconstructing $EM(T)$ from spectroscopic and narrow-band observations is non-trivial, with different inversion methods often giving significantly different results (Landi et al. 2012; Guennou et al. 2013; Aschwanden et al. 2015).

An important parameter for any proposed coronal heating mechanism is the frequency of energy release along a single magnetic strand, where the observed loop comprises many such strands. Nanoflare heating can be classified as being either a *high-* or *low-frequency*. In the case of high-frequency (HF) heating, t_N , the time between successive events, is such that $t_N \ll \tau_{cool}$, where τ_{cool} is a characteristic loop cooling time, and in the case of low-frequency (LF) heating $t_N \gg \tau_{cool}$ (Mulu-Moore et al. 2011; Warren et al. 2011; Bradshaw et al. 2012; Reep et al. 2013; Cargill et al. 2015). Steady heating is just high-frequency heating in the limit $t_N \rightarrow 0$. While a determination of t_N is of great importance, its measurement is challenging. For example, while direct observations of possible reconnection-associated heating through short timescale changes in loop structure and emission is feasible, as demonstrated by the Hi-C rocket flight (Cirtain et al. 2013; Cargill 2013), longer duration observations are required to constrain t_N . The previously-mentioned difficulties in reconstructing $EM(T)$ must also be borne in mind. Efforts to measure the heating frequency using narrow-band observations of intensity fluctuations in AR cores have proved similarly difficult (Ugarte-Urra & Warren 2014).

The use of hydrodynamic loop models, combined with sophisticated forward modeling, is a useful method for assessing a wide variety of heating scenarios. Such models of nanoflare-heated loops have found emission measure slopes consistent with those derived from observations in the temperature range $T < T_m$. For example, while Bradshaw et al. (2012) found that the full range of a could not be accounted for with low-frequency nanoflares, Reep et al. (2013) showed that using a tapered nanoflare train allowed for $0.9 \lesssim a \lesssim 4.5$. Cargill (2014), using a 0D loop model, investigated a large range of heating frequencies, $250 < t_N < 5000$ s, and found that only when t_N was between a few hundred and 2000 seconds and proportional to the nanoflare energy could the full range of observed emission measure slopes be found.

An analogous approach can be used to investigate the properties of the “hot” coronal component expected from nanoflare heating, and is the subject of the present series of papers. In Barnes et al. (2016) (Paper I, hereafter), we looked at the hot plasma properties due to a single isolated nanoflare. The effects of heating pulse duration, changes to conductive cooling due to heat flux

limiting, differential heating of electrons and ions, and non-equilibrium ionization (NEI) were studied. It was shown that signatures of nanoflare heating are likely to be found in the temperature range $4 \lesssim T \lesssim 10$ MK. The prospect of measurable signatures above 10 MK was found to be diminished for short heating pulses (with duration < 100 s), NEI, and differential heating of the ions rather than the electrons. It is important to stress for a single nanoflare that while the “hot” plasma is present, it cannot actually be detected.

However, nanoflare heating requires that we consider a “train” of nanoflares along a magnetic strand (Viall & Klimchuk 2011; Warren et al. 2011; Reep et al. 2013; Cargill et al. 2015). While a single nanoflare in the LF heating scenario will always occur in a plasma of characteristic AR density ($\sim 10^9 \text{ cm}^{-3}$), with significant consequences. In this paper, we use an efficient two-fluid hydrodynamic model to explore the effect of a nanoflare train with varying t_N on $EM(T)$, in particular for $T > T_m$. Preferential species heating, NEU, power-law nanoflare distributions, and the effects of a variable t_N between events are considered and an emission measure ratio metric, similar to that discussed in Brosius et al. (2014), is used to characterize the various results. Section 2 discusses the numerical model we have used to conduct this study and the parameter space we have investigated. Section 3 shows the resulting emission measure distributions and diagnostics for the entire parameter space. In Section 4, we discuss the impacts of two-fluid effects, pre-nanoflare density, and NEI on these calculated observables and how they may be interpreted in the context of nanoflare heating. Finally, Section 5 provides some concluding comments on our findings.

2. METHODOLOGY

2.1. Numerical Model

1D hydrodynamic models are excellent tools for computing field-aligned quantities in coronal loops. However, because of the small cell sizes needed to resolve the transition region and consequently small timesteps demanded by thermal conduction, the use of such models in large parameter space explorations is made impractical by long computational runtimes (Bradshaw & Cargill 2013). We use the popular 0D enthalpy-based thermal evolution of loops (EBTEL) model (Klimchuk et al. 2008; Cargill et al. 2012a,b, 2015) in order to efficiently simulate the evolution of a coronal loop over a large parameter space. This model, which has been successfully benchmarked against the 1D hydrodynamic HYDRAD code of Bradshaw & Cargill (2013), computes, with very low computational overhead, time-dependent, spatially-averaged loop quantities.

In order to treat the evolution of the electron and

ion populations separately, we use a modified version of the usual EBTEL equations. This amounts to computing spatial averages of the two-fluid hydrodynamic equations over both the transition region and corona. A full description and derivation of these equations can be found in the appendix of [Paper I](#). The relevant two-fluid pressure and density equations are,

$$\frac{d}{dt}\bar{p}_e = \frac{\gamma-1}{L} [\psi_{TR} - (\mathcal{R}_{TR} + \mathcal{R}_C)] + k_B \bar{n} \nu_{ei} (\bar{T}_i - \bar{T}_e) + (\gamma-1) \bar{Q}_e, \quad (1)$$

$$\frac{d}{dt}\bar{p}_i = -\frac{\gamma-1}{L} \psi_{TR} + k_B \bar{n} \nu_{ei} (\bar{T}_e - \bar{T}_i) + (\gamma-1) \bar{Q}_i, \quad (2)$$

$$\frac{d}{dt}\bar{n} = \frac{c_2(\gamma-1)}{c_3\gamma L k_B \bar{T}_e} (\psi_{TR} - F_{ce,0} - \mathcal{R}_{TR}), \quad (3)$$

where $c_2 = \bar{T}_e/T_{e,a} \approx 0.9$, $c_3 = T_{e,0}/T_{e,a} \approx 0.6$, ν_{ei} is the electron-ion binary Coulomb collision frequency and ψ_{TR} is a term included to maintain charge and current and neutrality. Additionally, $c_1 = \mathcal{R}_{TR}/\mathcal{R}_C$ and its formulation is discussed in [Cargill et al. \(2012a\)](#) with additional corrections detailed in Appendix 1 of [Paper I](#). These equations are closed by the equations of state $p_e = k_B n T_e$ and $p_i = k_B n T_i$. In the cases where we treat the plasma as a single-fluid, we use the original EBTEL model as described in [Klimchuk et al. \(2008\)](#); [Cargill et al. \(2012a\)](#).

The loop is heated by a prescribed heating function, applied to either the electrons (\bar{Q}_e) or the ions (\bar{Q}_i). Both species cool through a combination of thermal conduction ($F_{ce,0}$, $F_{ci,0}$) and an enthalpy flux to the lower atmosphere, with the electrons also undergoing radiative cooling (\mathcal{R}_C). In the case of conductive cooling, a flux limiter, $F = (1/2) f n k_B T V_e$, is imposed to mitigate runaway cooling in a low-density, high-temperature plasma. In all cases we use a saturation limit of $f = 1$. See [Paper I](#) for a discussion of how f is likely to effect the presence of hot emission in a nanoflare-heated plasma.

2.2. Energy Budget

We define our heating function in terms of a series of discrete heating events plus a static background heating to ensure that the loop does not drop to unphysically low temperatures and densities between events. For a triangular heating pulse of duration τ injected into a loop of half-length L and cross-sectional area A , the total event energy is $\varepsilon = LAH\tau/2$, where H is the heating rate. Each model run will consist of N heating events, each with peak amplitude H_i , and a steady background heating of $H_{bg} = 3.5 \times 10^{-5} \text{ erg cm}^{-3} \text{ s}^{-1}$.

Recent observations have suggested that loops in AR cores are maintained at an equilibrium temperature of $T_m \approx 4 \text{ MK}$ ([Warren et al. 2011, 2012](#)). Using our modified two-fluid EBTEL model, we have estimated the

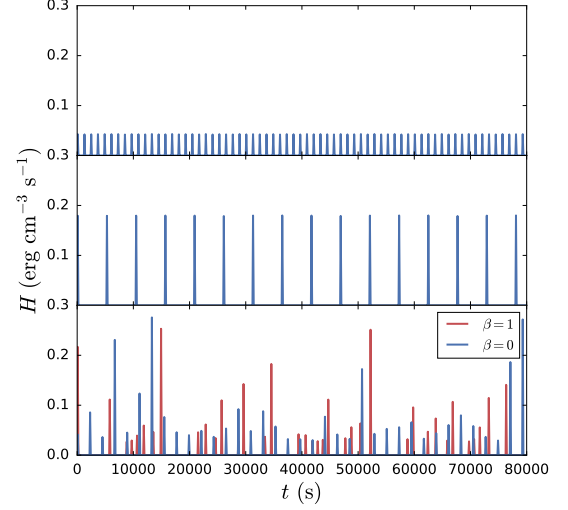


Figure 1. **Top:** Uniform heating amplitudes for $t_N = 1000$ s; **Middle:** Uniform heating amplitudes for $t_N = 5000$ s; **Bottom:** Heating amplitudes drawn from a power-law distribution with index $\alpha = -1.5$. The events shown in red have wait times that depend on the previous event energy while the events shown in blue have uniform wait times. The mean wait time in both cases is $t_N = 2000$ s.

time-averaged volumetric heating rate needed to keep a loop of half-length $L = 40 \text{ Mm}$ at $\bar{T} \approx 4 \text{ MK}$ as $H_{eq} \sim 3.6 \times 10^{-3}$. In the single-fluid EBTEL model, this value is slightly lower because losses due to electron-ion collisions are ignored. Thus, to maintain an emission measure peaked about T_m , for triangular pulses, the individual event heating rates are constrained by

$$H_{eq} = \frac{1}{t_{total}} \sum_{i=1}^N \int_{t_i}^{t_i+\tau} dt Q(t) = \frac{\tau}{2t_{total}} \sum_{i=1}^N H_i, \quad (4)$$

where t_{total} is the total simulation time. Note that if $H_i = H_0$ for all i , the heating rate for each event is $H_i = H_0 = 2t_{total}H_{eq}/N\tau$. Thus, for $L = 40 \text{ Mm}$, $A = 10^{14} \text{ cm}^2$, the average energy per event for a loop heated by $N = 20$ nanoflares in $t_{total} = 8 \times 10^4 \text{ s}$ is $\varepsilon = LA t_{total} H_{eq}/N \approx 5.8 \times 10^{24} \text{ erg}$, consistent with the energy budget of the Parker nanoflare model.

We define the heating frequency in terms of the waiting time, t_N , between successive heating events. Following [Cargill \(2014\)](#), the range of waiting times is $250 \leq t_N \leq 5000 \text{ s}$ in increments of 250 s, for a total of 20 different possible heating frequencies. Additionally, t_N can be written as $t_N = (t_{total} - N\tau)/N$, where we fix $t_{total} = 8 \times 10^4 \text{ s}$ and $\tau = 200 \text{ s}$. Note that because t_{total} and τ are fixed, as t_N increases, N decreases. Correspondingly, $\varepsilon_i = LA\tau H_i/2$, the energy injected per event, increases according to [Equation 4](#) such that the total energy injected per run is constant.

According to the nanoflare heating model of [Parker \(1988\)](#), turbulent loop footpoint motions twist and stress the field, leading to a buildup and subsequent release of

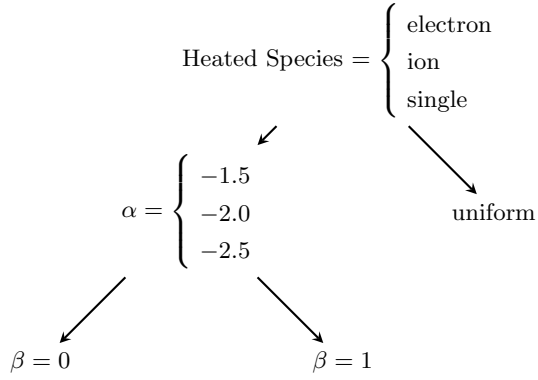


Figure 2. Total Parameter space covered. “single” indicates a single-fluid model. α is the power-law index and β indicates the scaling in the relationship $Q \propto T_N^\beta$, where $\beta = 0$ corresponds to the case where t_N and the event energy are independent. Note that $(3 \alpha \text{ values}) \times (2 \beta \text{ values}) + \text{uniform heating} = 7$ different types of heating functions.

energy. Following Cargill (2014), we let $\varepsilon_i \propto t_{N,i}^\beta$, where $\varepsilon_i, t_{N,i}$ are the total energy of event i and waiting time following event i , respectively, and $\beta = 1$ such that the event energy scales linearly with the waiting time. The reasoning for such an expression is as follows. Bursty, nanoflare heating is thought to arise from the stressing and subsequent relaxation of the coronal field. If a sufficient amount of energy is released into the loop, the field will need enough time to “unravel” and “wind up” again before the next event such that the subsequent waiting time is large. Conversely, if only a small amount of energy is released, the field will require a shorter unwinding time, resulting in a shorter interval between the subsequent events. Thus, this scaling provides a way to incorporate a more physically motivated heating function into a hydrodynamic model which cannot self-consistently determine the heat input based on the evolving magnetic field. Figure 1 shows the various heating functions used for several example t_N values.

2.3. Heating Statistics

We compute the peak heating rate per event in two different ways: 1) the heating rate is uniform such that $H_i = H_0$ for all i and 2) H_i is chosen from a power-law distribution with index α where $\alpha = -1.5, -2.0$, or -2.5 . For the second case, it should be noted that, when $t_N \approx 5000$ s, $N \sim 16$ events, meaning the events from a single run do not accurately represent the distribution of index α . Thus, a sufficiently large number of runs, N_R , are computed for each t_N to ensure that the total number of events is $N_{tot} = N \times N_R \sim 10^4$ such that the distribution is well-represented. Figure 2 shows the parameter space we will explore. For each set of parameters and waiting time t_N , we compute the resulting emission measure distribution for N events in a period t_{total} . This procedure is repeated N_R times until

$N \times N_R \sim 10^4$ is satisfied. Thus, when $t_N = 5000$ s and $N \sim 16$, $N_R = 625$, meaning the model is run 625 times with a heating frequency of $t_N = 5000$ s in order to properly fill out the event energy distribution.

2.4. Non-equilibrium Ionization

When considering the role of nanoflares in the production of hot plasma in AR cores, it is important to take non-equilibrium ionization (NEI) into account (Bradshaw & Cargill 2006; Reale & Orlando 2008). In a steady heating scenario, the ionization state is an adequate measure of the electron plasma temperature. Because the heating timescale is long (effectively infinite), the ionization state has plenty of time to come into equilibrium with the electron temperature.

In a nanoflare train, when the heating frequency is high, the loop is not allowed to drain or cool sufficiently between events, meaning the ionization state is kept at or near equilibrium. However, as the heating frequency decreases, the loop is allowed to cool and drain more and more during the inter-event period. If the heating occurs on a short enough timescale, the ionization state will not be able to reach equilibrium with the electron plasma before the loop undergoes rapid cooling by thermal conduction. Furthermore, if the frequency is sufficiently low so as to allow the loop to drain during the inter-event period, the ionization equilibrium timescale will increase. Thus, in the context of intermediate- to low-frequency nanoflares, NEI should be considered.

As in Paper I, we use the numerical code¹ outlined in Bradshaw (2009) to assess the impact of NEI on our results. Given a temperature ($T(t)$) and density ($n(t)$) profile from EBTEL, we compute the non-equilibrium ionization states for Fe IX through XXVII and the corresponding effective electron temperature, T_{eff} , that would be inferred by assuming ionization equilibrium. Using T_{eff} , we are then able to compute a corresponding NEI emission measure distribution, $EM(T_{eff})$.

3. RESULTS

We now show the results of our nanoflare train simulations for each point in our multidimensional parameter space: species heated (single-fluid, electron or ion), power-law index (α), heating frequency (t_N), and waiting-time/event energy relationship (β). In each 0D hydrodynamic simulation, a loop of half-length $L = 40$ Mm is heated by N triangular events of duration $\tau = 200$ s and peak heating rate H_i for a duration of $t_{total} = 8 \times 10^4$ s. The average interval between subsequent events is t_N (in the uniform and $\beta = 0$ cases,

¹ This code has been made freely available by the author and can be downloaded at: <https://github.com/rice-solar-physics/IonPopSolver>.

$t_{N,i} = t_N$ exactly for all i). We focus primarily on the emission measure distribution, $EM(T)$, and observables typically calculated from $EM(T)$. In all cases, the coronal emission measure is calculated according to the method outlined in section 3 of [Paper I](#). The corresponding NEI results, $EM(T_{eff})$, are calculated similarly, but using T_{eff} (see [Subsection 2.4](#)) instead of T . All results were processed using the IPython system for interactive scientific computing in Python ([Pérez & Granger 2007](#)) as well as the NumPy and Scipy numerical and scientific Python libraries ([van der Walt et al. 2011](#)). All results were visualized using the matplotlib graphics library ([Hunter 2007](#)).

3.1. Emission Measure Distributions

In our first set of results, we compare $EM(T)$ for three different types of heating functions, across six different heating frequencies. [Figure 3](#), [Figure 4](#), and [Figure 5](#) show the emission measure distributions in the single-fluid case, electron heating case, and ion heating case, respectively. Each panel in each figure corresponds to a different waiting time (t_N) and includes three different types of heating functions: uniform heating events (red), events chosen from a power-law distribution of index $\alpha = -2.5$ ($\beta = 0$ case, blue), and events chosen from a power-law distribution of index $\alpha = -2.5$ where the time between successive events depends on the heating rate of the preceding event ($\beta = 1$ case, green). Note that in all three figures, we show the results for only a single power-law index, $\alpha = 2.5$. Furthermore, the dashed lines denote the corresponding NEI cases, $EM(T_{eff})$. The cases shown in [Paper I](#) correspond approximately to the red curves in the lower right panels ($t_N = 5000$ s) of each of the three figures since the loop is allowed to cool and drain completely before reheating and a single nanoflare energy is used.

In [Subsection 2.3](#), we noted that for heating functions using a power-law energy distribution, for each t_N , we run the model N_R times. Thus, for each point in our parameter space, we produce N_R $EM(T)$ curves. In order to present our results compactly, the solid lines in [Figure 3](#), [Figure 4](#), and [Figure 5](#) each show the mean $EM(T)$ over all N_R curves. The shading represents 1σ from the mean. In this way, we account for the variations that may occur because of a lack/excess of strong heating events due to limited sampling from the distribution.

We look first at $EM(T)$ for the single-fluid case, [Figure 3](#). Firstly, as expected from [Cargill \(2014\)](#), as t_N increases, $EM(T)$ widens, extending to both cooler (< 4 MK) and hotter (> 4 MK) temperatures. The extension toward cooler temperatures arises because as t_N increases there is more time between successive heating events so that the loop so that the loops cools to

lower temperatures before being reheated. The dependence on α and β is similar to that described in [Cargill \(2014\)](#). The uniform (red) and $\beta = 0$ (blue) $EM(T)$ curves evolve similarly as they extend to cooler temperatures with increasing t_N while the $\beta = 1$ curves (green) extend to cooler temperatures much more rapidly. For example, at $t_N = 1500$ s, both the uniform and $\beta = 0$ cases show little to no emission below 2 MK while the $\beta = 1$ cases extends to temperatures well below 1 MK ([Cargill 2014](#)). As in [Paper I](#), the results below T_m are relatively independent of which species is heated.

The behavior of $EM(T)$ above T_m is more complicated. For small t_N , the emission measure distribution falls off sharply on the hot side for a uniform nanoflare train but a power law distribution leads to a broader distribution above T_m . This just reflects the different initial temperatures generated with a power-law distribution since $T \simeq H^{2/7}$. As t_N increases, the distribution for uniform heating gradually broadens as the initial temperature rises due to the lower density in which the heating occurs. A similar broadening occurs for the power laws with the $\beta = 0$ and $\beta = 1$ results showing little difference. Note that the $\beta = 0$ curve is barely visible as it overlaps almost completely with the $\beta = 1$ curve. Especially interesting in this case are the results with NEI included. For a uniform nanoflare train, NEI plays no role up to $t_N = 2500$ sec, but above that it restricts the temperatures that can be detected, as shown in [Paper I](#). This hot emission is relocated to cooler temperatures, resulting in a “bump” in the emission measure distribution near 10 MK. On the other hand, NEI plays almost no role in the power law distributions, in both the $\beta = 1$ and $\beta = 0$ cases.

From these initial results, there is an important difference in the information available in potential observations. Below T_m the value of a requires a specific form of the waiting time between nanoflares which in turn informs about the nature of energy release ([Cargill 2014](#)). Above T_m , there is no information about the role of a waiting time, but the emission measure distribution does inform about the need for a power-law energy distribution and the density in which the nanoflare occurs. Taken together, the overall conclusion is the same: nanoflares require an *intermediate frequency*.

For electron heating, the $EM(T)$ curves for the different types of heating functions shown in [Figure 4](#) evolve similarly to those shown in [Figure 3](#), especially on the cool side where the density is sufficiently high such that the electrons and the ions to equilibrate. On the hot side, for $t_N \leq 750$ s, the electron and single-fluid cases are quite similar. However, for $t_N \geq 1500$ s, in the electron heating case, $EM(T)$ steepens just above 4 MK and then flattens out near 10 MK. This change in shape is most obvious in the uniform heating case where a dis-

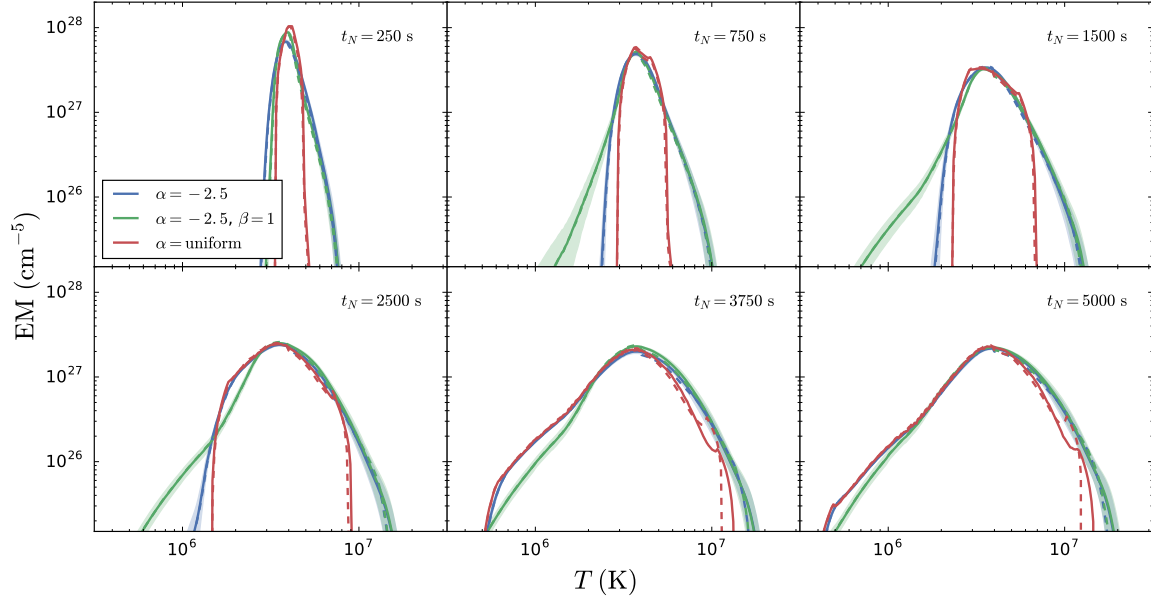


Figure 3. Emission measure distributions for waiting-times $t_N = 250, 750, 1500, 2500, 3750, 5000$ s in the single-fluid case. The three types of heating functions shown are uniform heating rates (red), heating rates chosen from a power-law distribution of $\alpha = -2.5$ (blue), and heating rates chosen from a power-law distribution of $\alpha = -2.5$ where the time between successive events is proportional to the heating rate of the preceding event (green). The solid lines in the two power-law cases show the mean $EM(T)$ over N_R runs and the shading indicates 1σ from the mean. The dashed lines denote the corresponding $EM(T_{eff})$ distribution. The standard deviation is not included in the NEI results.

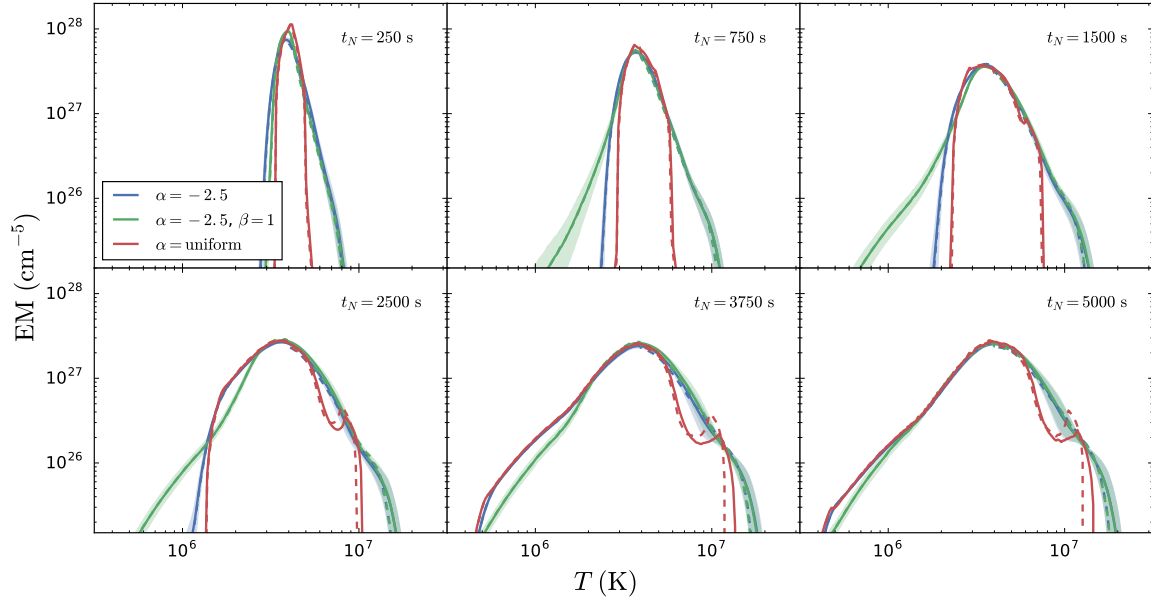


Figure 4. Same as Figure 3, but for the case where only the electrons are heated.

411 tinct “hot shoulder” forms just above 10 MK. In the
 412 power-law cases, this feature is less pronounced though
 413 $EM(T)$ extends to slightly higher temperatures. The
 414 conclusions regarding the role of NEI are similar to those
 415 in the single-fluid case: it is not a factor when the heating
 416 rates are determined by a power-law. In the uniform
 417 case, the hot emission is again truncated and relocated
 418 to cooler temperatures, with more pronounced “bump”

419 in the $EM(T)$ near 10 MK.

420 When only the ions are heated (Figure 5), the cool side
 421 of the $EM(T)$ is again very similar to both the single-
 422 fluid and electron heating cases due to equilibration. On
 423 the hot side, for intermediate to low heating frequencies
 424 (i.e. $t_N \geq 1500$ s), the $EM(T)$ in the uniform heating
 425 case is truncated below 10 MK and in the power-law
 426 cases extends to just above 10 MK for the lowest heating

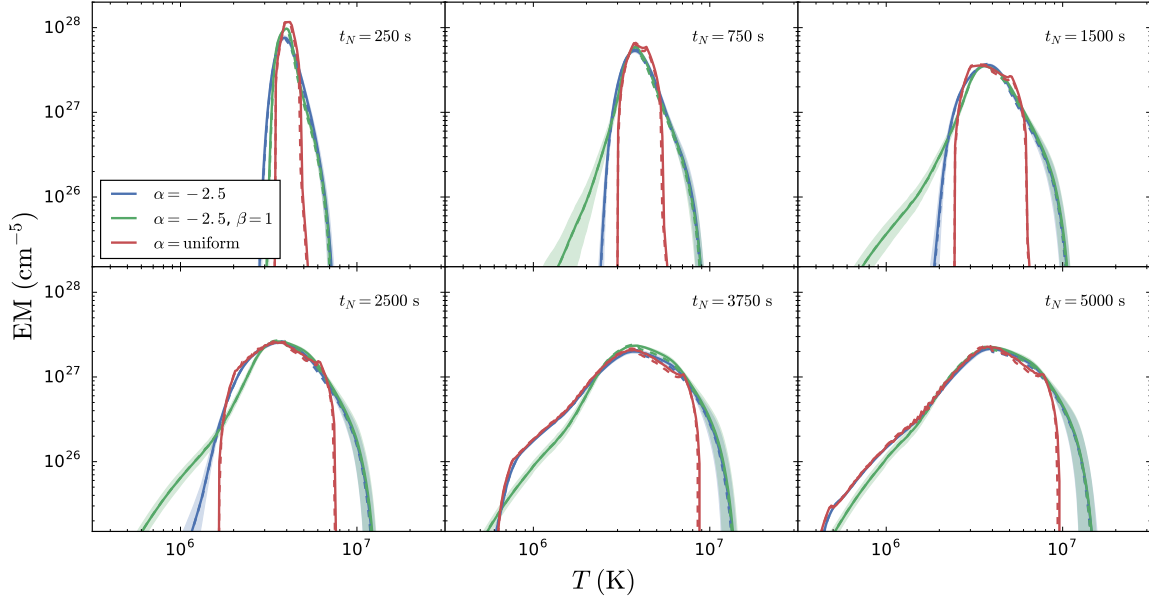


Figure 5. Same as Figure 3, but for the case where only the ions are heated.

frequency ($t_N = 5000$ s). This cutoff at lower temperatures is due to the fact that electrons cannot “see” the ions until they have cooled well below their peak temperature. This is discussed in Paper I though in the single-pulse cases, the cutoff occurred at lower temperatures. Additionally, in both the uniform and power-law cases, the peak of $EM(T)$ is wider for these low frequencies compared to those cases shown in the lower right panels of Figure 3 and Figure 4. Regarding the role of NEI, there is no significant difference between $EM(T)$ and $EM(T_{eff})$ for either the uniform or power-law cases. Here the electrons are essentially heated on a timescale dictated by the Coulomb collision frequency which is slow enough to ensure ionization equilibrium throughout the heating and conductive cooling phases.

3.2. Pre-nanoflare Density

In Cargill (2014), Paper I, and Subsection 3.1, we have suggested that the plasma density prior to the nanoflare occurring is a crucial parameter in determining the emission measure distribution. This arises in two distinct ways. Below T_m , the temperature and density at which the nanoflare occurs cuts off the emission at lower temperatures. When combined with an energy-dependent waiting time, this can lead to a range of EM slopes in this region (Cargill 2014). Above T_m , the initial density determines the temperature increase due to the nanoflare, how quickly the initial hot plasma cools, and whether NEI effects are important. We now examine this further.

In the single-fluid and electron heating cases, while $EM(T)$ in the uniform and power-law heating cases generally agree for low-frequency heating ($t_N = 5000$ s), for

intermediate frequencies ($t_N \approx 750 - 2500$ s), the power-law cases show an enhanced high-temperature component compared to the uniform case as seen in Figure 3 and Figure 4. Figure 6 shows sample heating, temperature, and density profiles for an intermediate heating frequency ($t_N = 2500$ s), in the case where only the electrons are heated, for the three different types of heating functions. In the uniform heating rate case (red), each event has a maximum heating rate of H_0 such that the loop undergoes $N \approx 30$ identical heating and cooling cycles, each time reaching a maximum temperature and density of $T_{max,0}$ and $n_{max,0}$, respectively.

In comparing various heating models, we insist that the total energy injected into the loop is the same for each run (see Equation 4). When the nanoflare heating rates are distributed according to a power-law, there will be many events where $H_i < H_0$ and a few events where $H_i \gg H_0$. These few high energy events lead to $T \gg T_{max,0}$ (blue and green curves) as seen in the middle panel of Figure 6. Because these events are injected into a plasma that is sufficiently dense due to the draining and cooling times being longer than the time since the previous event, the emission measure is able to “see” these hot temperatures, resulting in a > 10 MK component of $EM(T)$ (see lower left panel of Figure 3 and Figure 4). In the uniform case, $T_{max,0} < 10$ MK such that $EM(T)$ has a steep cutoff right at 10 MK. Additionally, we note that the only effect of the longer wait times in the $\beta = 1$ case as compared to the $\beta = 0$ case is an extended cool emission measure at intermediate frequencies (e.g. $t_N = 2500$ s); the hot part of $EM(T)$ for both power-law cases is nearly identical. Thus, the hot and cool sides of the emission measure distribution

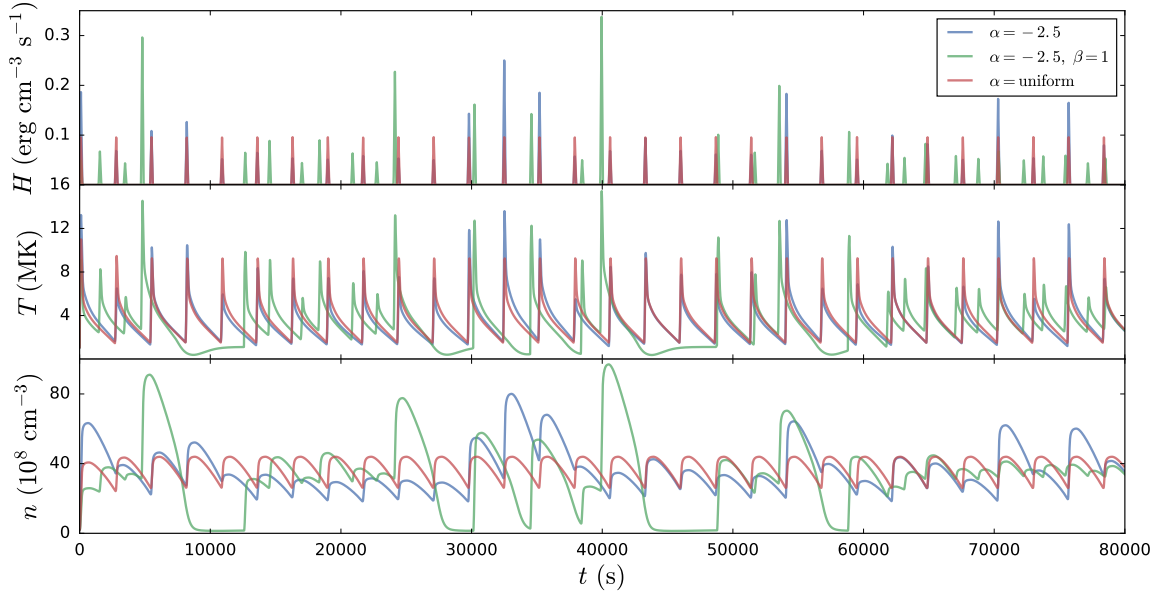


Figure 6. Example heating (top), temperature (middle), and density (bottom) profiles for the case in which only the electrons are heated with an intermediate heating frequency of $t_N = 2500$ s. The three curves shown in each panel correspond to uniform heating rates (red), heating rates chosen from a power-law distribution of $\alpha = -2.5$ (blue), and heating rates chosen from a power-law distribution of $\alpha = -2.5$ where the time between successive events is proportional to the heating rate of the preceding event (green).

are largely isolated from one another as they are determined by separate phases of the loop evolution.

3.3. Hot Plasma Diagnostics

3.3.1. Emission Measure Slope

We now examine several observables often used to characterize the emission measure distribution. The most common observable is the emission measure slope a such that $\text{EM} \propto T^a$ for $10^{5.5} \leq T \leq 10^{6.6}$ K. Both observational and modeling studies have found that $2 \lesssim a \lesssim 5$ (see Table 3 of Bradshaw et al. 2012) and in particular, Cargill (2014) found that a heating function of the form $t_N \propto \varepsilon$ was needed in order to account for this range of slopes. Additionally, a similar scaling of $\text{EM} \propto T^{-b}$ for $10^{6.6} \leq T \leq 10^{7.0}$ has been claimed though measurements of b have been subject to large uncertainties (Warren et al. 2012).

Figure 7 shows an example of how both a and b can be calculated from the cool and hot sides of $\text{EM}(T)$, respectively. We select a single sample run from our parameter space in which only the electrons are heated by nanoflares from a power-law distribution of $\alpha = -2.5$ and spaced uniformly by an interval of $t_N = 5000$ s. We calculate the resulting $\text{EM}(T)$ and fit $\log \text{EM}$ to $a \log T$ on $\log T_{c,\min} < \log T < \log T_{c,\max}$ and $-b \log T$ on $\log T_{h,\min} < \log T < \log T_{h,\max}$ using the Levenburg-Marquardt algorithm for least-squares curve fitting as implemented in the SciPy scientific Python package (van der Walt et al. 2011). We fix the lower limit on each interval such that $T_{c,\min} = 10^{5.7}$ K and $T_{h,\min} = 10^{6.7}$

K and vary the upper limits over $10^{6.1} < T_{c,\max} < 10^{6.5}$ K and $10^{6.8} < T_{h,\max} < 10^{7.2}$ K. The left panel of Figure 7 shows a (blue) and b (red) as a function upper limit of the fit interval, $T_{c,\max}$ (bottom axis) and $T_{h,\max}$ (top axis), respectively. The shading denotes the uncertainty of the fit. The right panel of Figure 7 shows the resulting fit lines superimposed on the emission measure distribution.

From the left panel of Figure 7, we see that, while a is relatively insensitive to the fit interval, b varies between approximately 2 and 4.5 depending on the choice of bounds. Furthermore, the uncertainty in the fitting procedure for b is relatively large, with the average uncertainty over the entire range of $T_{h,\max}$ being $\bar{\sigma}_b \approx 0.17$. Contrastingly, we find that $a \approx 2.3$ with little variation over all values of $T_{c,\max}$ considered here and that $\bar{\sigma}_a \approx 0.018$, nearly an order of magnitude smaller than $\bar{\sigma}_b$. The overlaid fit lines in the right panel of Figure 7 similarly show that while $\log \text{EM}$ is roughly linear over $5.7 < \log T < 6.5$, this is not the case for the interval $6.7 < \log T < 7.2$. In particular, a function of the form T^{-b} cannot describe the hot shoulder in the emission measure distribution near $10^{7.1}$ K.

Collaboration note: More discussion here? Some conclusions? What else do we need to say? Lead in to the next point a bit better? Maybe some discussion of why the slopes are different? What slopes we should expect? Refer to Paper 1...

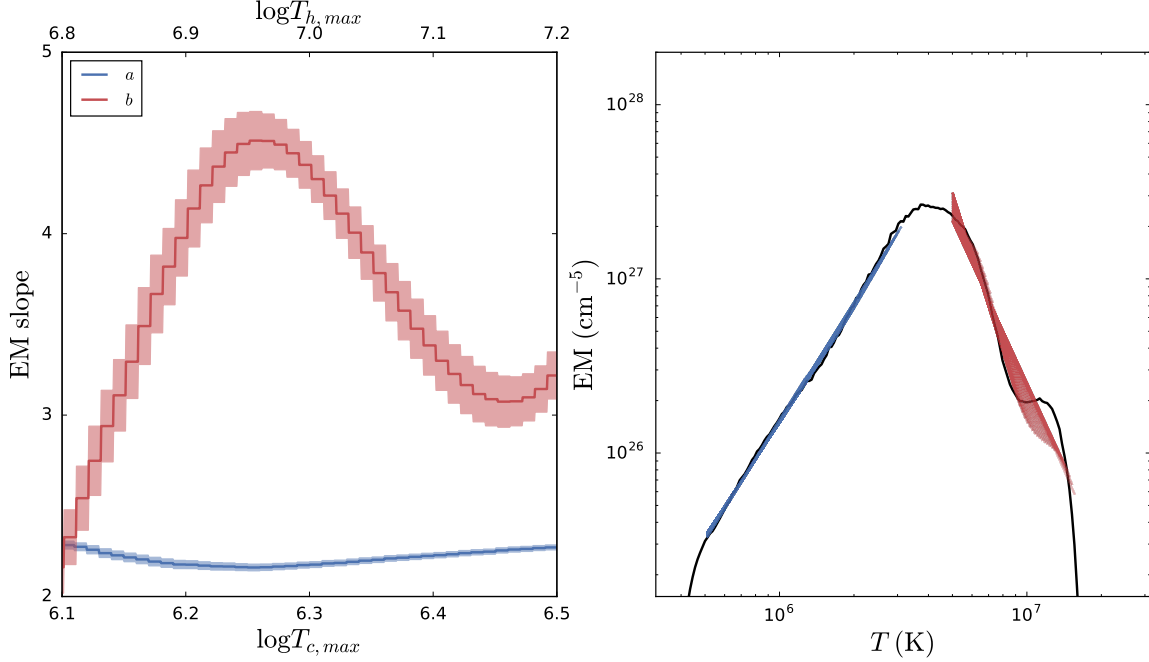


Figure 7. Fits to a sample emission measure distribution constructed from a loop plasma in which only the electrons were heated by events chosen from a power-law distribution with $\alpha = -2.5$ and equally spaced by an interval of $t_N = 5000$ s. **Left:** EM(T) slope as a function of upper bound on fit interval for both the hot (red) and cool (blue) side of EM(T). The shading denotes the uncertainty of the fit. The bottom axis corresponds to the varying upper limit on the fit to the cool side while the top axis corresponds to the varying upper limit on the fit to the hot side. **Right:** EM(T) with the overlaid hot (red) and cool (blue) fit lines whose slopes correspond to those shown on the left. The cool power-law fits describe EM(T) for $T < 4$ MK quite well while a similar fit on the hot side fails to accurately describe the shape of the emission measure distribution for $T > 4$ MK.

3.3.2. Emission Measure Ratio

Brosius et al. (2014), using observations of an active region from the *EUNIS-13* sounding rocket, found that the intensity ratio of Fe XIX (formed at $T \approx 10^{6.95}$ K) to Fe XII (formed at $T \approx 10^{6.2}$ K) is ~ 0.59 inside the AR core as compared to ~ 0.076 outside, providing possible evidence for impulsive heating. As a proxy for this intensity ratio and an alternative to the hot emission measure slope b , we propose using an emission measure ratio, $\text{EM}(T_{\text{hot}})/\text{EM}(T_{\text{cool}})$. Unlike an emission measure slope, a simple emission measure ratio gives information about the emission at only a single “hot” temperature relative to a single “cool” temperature. We choose $T_{\text{hot}} = 10^{6.95}$ K and $T_{\text{cool}} = 10^{6.3} \approx 2 \times 10^6$ K, the latter slightly higher (closer to $T_m \approx 4$ MK) than the formation temperature of Fe XII such that the emission measure ratio is less sensitive to variations in the cool emission and thus a more accurate measure of changes in the amount of hot plasma. The ratio of other emission lines could also be used.

Such an emission measure ratio also provides a way to compare in a concise way every point in our multidimensional parameter space while acknowledging that we are reducing 8×10^4 s of loop evolution to a single value. The left panel of Figure 8 shows the case in which only the electrons are heated, where each individual histogram

(denoted by linestyle and color) corresponds to a different type of heating function. This means, for example, that the solid blue histogram includes emission measure ratios for all values of t_N , but for only those cases where heating events are chosen from a power-law distribution of $\alpha = -1.5$ and $t_{N,i} = t_N$ for all i (i.e. $\beta = 0$). We see that the emission measure ratio is largely insensitive to α and is peaked sharply at approximately 0.25; the distribution peaks at slightly higher values for the $\beta = 1$ case though the overall shape of the distribution is the same. Here we have not included the uniform heating case due to small number statistics (i.e. < 20 emission measure ratios).

The right panel of Figure 8 shows these same emission measure ratios, but now separated by t_N . For example, the solid red histogram includes emission measure ratios for every type of heating function (i.e. uniform, all α and all β), but for only those runs where $t_N = 3000$ s. Note that we choose to only show results for five values of t_N for aesthetic purposes. We find that for $t_N \leq 3000$ s, the emission measure ratios are largely clustered below 0.5, with $t_N = 2000, 3000, 4000$ s peaking between $\sim 0.3 - 0.45$. For $t_N > 4000$ s, the emission measure ratio seems to be more sensitive to the heating frequency.

Similarly, we compute the same emission measure ratio for the case in which only the ions are heated. The

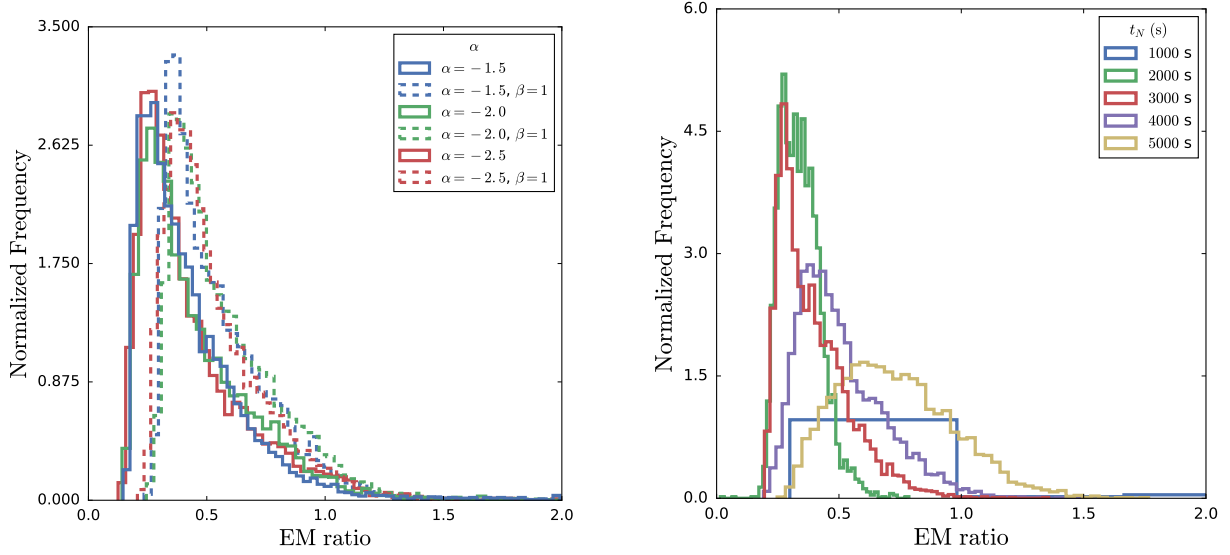


Figure 8. Histograms of emission measure ratios for all heating function types and heating frequencies for the case in which only the electrons are heated. In both panels each histogram is normalized such that for each distribution $P(x)$, $\int_{-\infty}^{\infty} dx P(x) = 1$ and the bin widths are calculated using the well-known Freedman-Diaconis formula (Freedman & Diaconis 1981). **Left:** Emission measure ratios separated by heating function type. **Right:** Emission measure ratios separated by waiting time, t_N . For aesthetic purposes, only five values of t_N are shown.

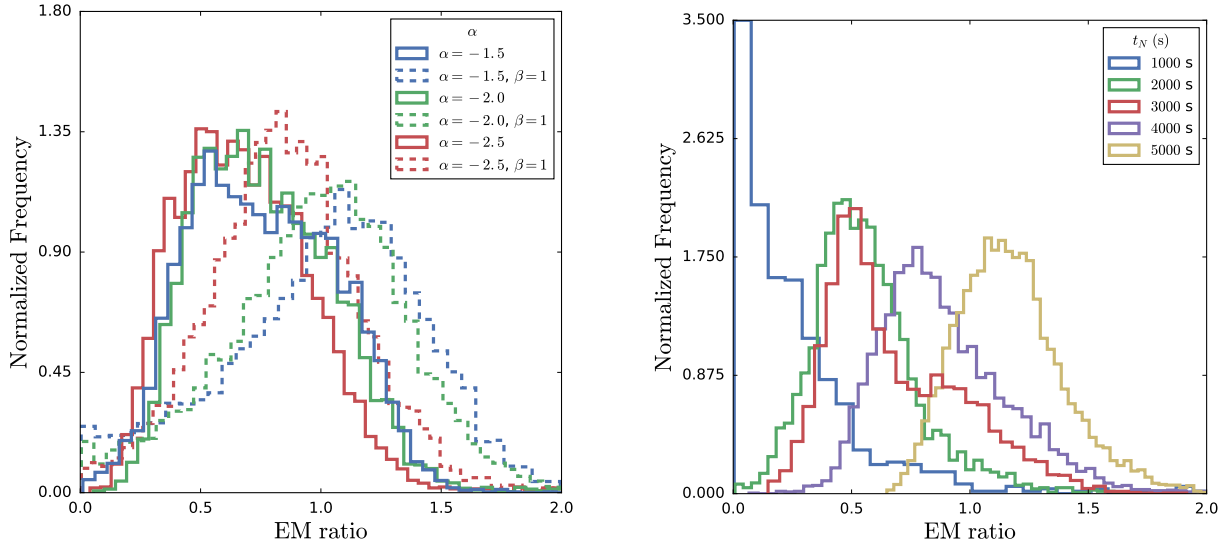


Figure 9. Same as Figure 8, but for the case where only the ions are heated.

left panel of Figure 9 shows histograms for each type of heating function. Similar to the electron heating results, we find that the $\beta = 0$ distributions peak at lower values compared to the $\beta = 1$ distributions and that in the $\beta = 0$ case, the distribution of emission measure ratios is relatively insensitive to α . However, unlike the electron heating case, the distributions in all cases are much wider and peak at higher values, ~ 0.5 for $\beta = 0$ and > 1 for $\beta = 1$. Furthermore, in the $\beta = 1$ case, the $\alpha = -2.5$ distribution peaks at lower values compared $\alpha = -1.5, -2.0$. The right panel of Figure 9 shows

the same emission measure ratios now grouped by waiting time where again we only show five values of t_N . With the exception of the $t_N = 2000$ s and $t_N = 3000$ s group, the distributions for each value of t_N are much more spread out (as compared Figure 8). In particular, $t_N = 5000$ s peaks above 1.0 and extends past 1.5 while $t_N = 1000$ s peaks near 0 and drops off very steeply before 0.5. In general, the emission measure ratios in the ion heating case appear to be more sensitive to t_N compared to the electron heating case.

Collaboration note: More interpretation here?

Discuss conceptually the implication(s) of some of these results.

4. DISCUSSION

1. *Collaboration note: > 10 MK present in nanoflare train runs relative to single pulse results from paper I*
2. *Collaboration note: consistency of results with Cargill (2014) on the cool side; unsuitability of the hot emission measure slope*
3. *Collaboration note: importance of density preconditioning in departures from IEQ*
4. *Collaboration note: emission measure ratio results in light of Brosius et al, 2014*
5. *Collaboration note: can we say something about possible heating frequencies? likelihood of electron heating over ion heating?*

Collaboration note: Adding this paragraph here for now. Maybe chop up and incorporate into discussion or delete altogether Another important difference between the uniform and power-law cases is the impact of NEI on the hot part of $EM(T)$. Recall from Subsection 2.2 that the uniform heating rate $H_0 = 2t_{total}H_{eq}/N\tau = 2H_{eq}(t_N/\tau + 1)$. From the top panel of Figure 6 we see that in the power-law case, the heating rate can be as high as $H_i \sim 0.3 \text{ erg cm}^{-3} \text{ s}^{-1}$. In terms of a uniform heating rate, this corresponds to a waiting time of $t_N \approx 8100 \text{ s}$. So even for the lowest heating frequency in the uniform case, the heating rate

is still much lower. Furthermore, for $t_N = 5000 \text{ s}$, the lowest heating frequency considered here, the loop is allowed to drain to its equilibrium value (as determined by the background heating) between each event such that events with a heating rate $H_0 \approx 0.2 \text{ erg cm}^{-3} \text{ s}^{-1}$ are injected into a low-density loop, meaning that the ionization state will not be able to keep pace with the subsequently rapid rise in temperature, resulting in $EM(T_{eff})$ having a lower temperature cutoff. On the other hand, when the heating events are selected from a power-law distribution, events with $H_i > 0.2 \text{ erg cm}^{-3} \text{ s}^{-1}$ can be injected into a much higher density loop (because lower values of t_N prevent longer draining times). This allows the ionization state to be relatively representative of the electron temperature such that $EM(T) \approx EM(T_{eff})$.

5. CONCLUSIONS

WTB was provided travel support to the Coronal Loops Workshop VII held in Cambridge, UK, July 21–23, 2015, at which a preliminary version of this work was presented, by NSF award number 1536094. This work was supported in part by the Big-Data Private-Cloud Research Cyberinfrastructure MRI-award funded by NSF under grant CNS-1338099 and by Rice University.

Software: IPython (Pérez & Granger 2007), Jupyter notebook, matplotlib (Hunter 2007), NumPy, seaborn (Waskom et al. 2016), Scipy (van der Walt et al. 2011)

REFERENCES

- Aschwanden, M. J., Boerner, P., Caspi, A., et al. 2015, *Solar Physics*, 290, 2733
- Barnes, W. T., Cargill, P. J., & Bradshaw, S. J. 2016, *The Astrophysical Journal*, in press
- Bradshaw, S. J. 2009, *Astronomy and Astrophysics*, 502, 409
- Bradshaw, S. J., & Cargill, P. J. 2006, *Astronomy and Astrophysics*, 458, 987
- . 2013, *The Astrophysical Journal*, 770, 12
- Bradshaw, S. J., Klimchuk, J. A., & Reep, J. W. 2012, *The Astrophysical Journal*, 758, 53
- Brosius, J. W., Daw, A. N., & Rabin, D. M. 2014, *The Astrophysical Journal*, 790, 112
- Cargill, P. 2013, *Nature*, 493, 485
- Cargill, P. J. 1994, *The Astrophysical Journal*, 422, 381
- . 2014, *The Astrophysical Journal*, 784, 49
- Cargill, P. J., Bradshaw, S. J., & Klimchuk, J. A. 2012a, *The Astrophysical Journal*, 752, 161
- . 2012b, *The Astrophysical Journal*, 758, 5
- Cargill, P. J., & Klimchuk, J. A. 2004, *The Astrophysical Journal*, 605, 911
- Cargill, P. J., Warren, H. P., & Bradshaw, S. J. 2015, *Philosophical Transactions of the Royal Society of London Series A*, 373, 20140260
- Cirtain, J. W., Golub, L., Winebarger, A. R., et al. 2013, *Nature*, 493, 501
- Del Zanna, G., & Mason, H. E. 2014, *Astronomy and Astrophysics*, 565, A14
- Del Zanna, G., Tripathi, D., Mason, H., Subramanian, S., & O’Dwyer, B. 2015, *Astronomy and Astrophysics*, 573, A104
- Freedman, D., & Diaconis, P. 1981, *Zeitschrift für Wahrscheinlichkeitstheorie und Verwandte Gebiete*, 57, 453
- Guenou, C., Auchère, F., Klimchuk, J. A., Bocchialini, K., & Parenti, S. 2013, *The Astrophysical Journal*, 774, 31
- Hunter, J. D. 2007, *Computing in Science & Engineering*, 9, 90
- Jordan, C. 1975, *Solar Gamma-, X-, and EUV Radiation*, 68
- Klimchuk, J. A. 2006, *Solar Physics*, 234, 41
- Klimchuk, J. A., Patsourakos, S., & Cargill, P. J. 2008, *The Astrophysical Journal*, 682, 1351
- Kosugi, T., Matsuzaki, K., Sakao, T., et al. 2007, *Solar Physics*, 243, 3
- Landi, E., Reale, F., & Testa, P. 2012, *Astronomy and Astrophysics*, 538, A111
- Miceli, M., Reale, F., Gburek, S., et al. 2012, *Astronomy and Astrophysics*, 544, A139
- Mulu-Moore, F. M., Winebarger, A. R., & Warren, H. P. 2011, *The Astrophysical Journal Letters*, 742, L6
- Parker, E. N. 1988, *The Astrophysical Journal*, 330, 474
- Petralia, A., Reale, F., Testa, P., & Del Zanna, G. 2014, *Astronomy and Astrophysics*, 564, A3
- Pérez, F., & Granger, B. E. 2007, *Computing in Science & Engineering*, 9, 21

- Reale, F., & Orlando, S. 2008, *The Astrophysical Journal*, 684, 715
- Reale, F., Testa, P., Klimchuk, J. A., & Parenti, S. 2009, *The Astrophysical Journal*, 698, 756
- Reep, J. W., Bradshaw, S. J., & Klimchuk, J. A. 2013, *The Astrophysical Journal*, 764, 193
- Schmelz, J. T., Asgari-Targhi, M., Christian, G. M., Dhaliwal, R. S., & Pathak, S. 2015, *The Astrophysical Journal*, 806, 232
- Schmelz, J. T., & Pathak, S. 2012, *The Astrophysical Journal*, 756, 126
- Schmelz, J. T., Saar, S. H., DeLuca, E. E., et al. 2009, *The Astrophysical Journal Letters*, 693, L131
- Testa, P., & Reale, F. 2012, *The Astrophysical Journal Letters*, 750, L10
- Testa, P., Reale, F., Landi, E., DeLuca, E. E., & Kashyap, V. 2011, *The Astrophysical Journal*, 728, 30
- Tripathi, D., Klimchuk, J. A., & Mason, H. E. 2011, *The Astrophysical Journal*, 740, 111
- Ugarte-Urra, I., & Warren, H. P. 2014, *The Astrophysical Journal*, 783, 12
- van der Walt, S., Colbert, S. C., & Varoquaux, G. 2011, *Computing in Science & Engineering*, 13, 22
- Viall, N. M., & Klimchuk, J. A. 2011, *The Astrophysical Journal*, 738, 24
- Warren, H. P., Brooks, D. H., & Winebarger, A. R. 2011, *The Astrophysical Journal*, 734, 90
- Warren, H. P., Winebarger, A. R., & Brooks, D. H. 2012, *The Astrophysical Journal*, 759, 141
- Waskom, M., Botvinnik, O., drewokane, et al. 2016, doi:10.5281/zenodo.45133
- Winebarger, A. R., Schmelz, J. T., Warren, H. P., Saar, S. H., & Kashyap, V. L. 2011, *The Astrophysical Journal*, 740, 2
- Winebarger, A. R., Warren, H. P., Schmelz, J. T., et al. 2012, *The Astrophysical Journal Letters*, 746, L17